RESEARCH ARTICLE | JANUARY 15 2025

Multi-functional terahertz nano-metasurface for beam-splitting and nonlinear resonance frequency shifting

Jianghao Li ; Jiahua Cai ; Chunyan Geng; Deyin Kong; Mingxuan Zhang ; Baogang Quan; Xianxun Yao; Guolin Sun ; Xiaojun Wu

Appl. Phys. Lett. 126, 021701 (2025)
https://doi.org/10.1063/5.0252621

Applied Physics Letters ARTICLE pubs.aip.org/aip/apl

Multi-functional terahertz nano-metasurface for beam-splitting and nonlinear resonance frequency shifting

Cite as: Appl. Phys. Lett. **126**, 021701 (2025); doi: 10.1063/5.0252621
Submitted: 11 December 2024 · Accepted: 7 January 2025 ·
Published Online: 15 January 2025

View Online Export Citation CrossMark

Jianghao Li,[1] Jiahua Cai,[1] Chunyan Geng,[1] Deyin Kong,[1,2] Mingxuan Zhang,[1] Baogang Quan,[3,4,5] Xianxun Yao,[1] Guolin Sun,[1,a)] and Xiaojun Wu[1,2,6,7,a)]

AFFILIATIONS

[1]School of Electronic and Information Engineering, Beihang University, Beijing 100191, China
[2]Zhangjiang Laboratory, Shanghai 201210, China
[3]Beijing National Laboratory for Condensed Matter Physics, Institute of Physics, Chinese Academy of Sciences, Beijing 100190, China
[4]Songshan Lake Material Laboratory, Guangdong 523808, China
[5]University of Chinese Academy of Sciences, Beijing 100049, China
[6]International Terahertz Research Center, Hangzhou International Innovation Institute, Beihang University, Hangzhou 311115, China
[7]Wuhan National Laboratory for Optoelectronics, Huazhong University of Science and Technology, Wuhan 430074, China

[a)]**Authors to whom correspondence should be addressed:** guolin.sun@buaa.edu.cn and xiaojunwu@buaa.edu.cn

ABSTRACT

The emergence of terahertz (THz) nanoscale resonance metasurface devices represents an innovative method for modulating THz waves by utilizing the intense, high-frequency alternating electric field in THz radiation. However, compared to traditional modulation methods that employ electrical, optical, and other techniques, the potential of these devices still necessitates further exploration. In this work, we achieved THz beam-splitting and field-induced nonlinear frequency shifting functions within a single THz nano-metasurface device. The device consists of single split-ring resonators (s-SRRs) with a nanogap on GaAs substrate. The pattern design based on the Pancharatnam–Berry (P-B) phase principle can split the incident wave into three beams. Meanwhile, its frequency shifting capability, which varies with the E-field, has been thoroughly investigated. The device performance was experimentally evaluated by an angle-resolved THz time-domain spectroscopy (THz-TDS) system and a strong-field THz-TDS system. This device could serve as a promising research platform for integrating THz with nano-optics and holds the potential for ultrafast modulation, offering application prospects in radar, wireless communication, and electromagnetic protection.

Terahertz (THz) modulators are key to the advancement of THz applications, among which resonance modulation stands out as one of the hot research topics. THz resonance metamaterials, with advantages such as ease of fabrication, low cost, and flexible design, have been widely used in the development of THz wave modulators[1–5] and sensors.[6–8] Traditional THz metasurface modulators mainly rely on active modulation methods,[9] including electrical,[10–12] optical,[13,14] and thermal mechanisms,[15–17] which involve relatively complex fabrication processes and experience limitations in modulation rates due to the inherent characteristics of the modulation mechanisms employed. On the other hand, self-modulation is a promising ultrafast modulation technique, in which researchers have already demonstrated ultrafast self-phase modulation[18] and absorption-based self-modulation.[19] This is achieved by leveraging THz pulses with picosecond-scale ultrashort pulse widths and nonlinear effects in semiconductor materials. The recently developed nanogap-based THz devices utilize the significant local field enhancement effect[20] at the gap to provide the high electric field sensitivity[21] required for this modulation and reduce the macroscopic incident THz E-field requirements to excite the nonlinear effects.[22] Meanwhile, with the development and widespread availability of strong-field THz radiation sources,[23–25] the implementation of this field-strength-dependent modulation technique has become increasingly feasible.

In this work, we have not only developed a multi-functional THz nanogap modulation device with ultrafast modulation potential, but

also further studied the self-modulating behavior of the resonance frequency. In addition, we have also detailed a cost-effective method for fabricating the 15-nm gaps. The nanogap single split-ring resonators (s-SRRs) on GaAs substrate can perform nonlinear resonance frequency shifts of up to 100 GHz, which exhibits a continuous variation with the THz electric field. The maximum frequency shift occurs at an incident electric field of about 160 kV/cm. With a pattern design based on the Pancharatnam–Berry (P-B) phase principle, the metasurface is also capable of splitting incident THz waves around 0.45 THz into three beams at designed angles under weak-field conditions. The two functions of the device have been evaluated by two self-built time-domain spectroscopy (TDS) systems. In addition, its ultrafast potential has been approved by a THz-pump THz-probe technique. Our developed device represents a significant advancement in the development of THz self-modulation devices, serves as an experimental platform for investigating the interaction between THz and nano-optics across a wide range of electric fields, with potential applications spanning various fields, including radar systems, mobile communications, and electromagnetic protection.

The THz beam-splitting nano-metasurface was designed to effectively split and redirect THz waves within a specified frequency range at precise angles, as illustrated in Fig. 1(a). Constructed on a GaAs substrate, the device featured a square arrangement of s-SRRs, characterized by a nanogap width of merely 15 nm. The transmission spectrum manifests distinct resonance frequencies when the electric field of the incident wave polarized along the arm with the gap (TM-polarized) and perpendicular to the arm (TE-polarized), f_1 and f_2, respectively. Particularly, upon the incidence of TM-polarized strong-field THz waves, the localized field enhancement effect at the nanogap excites

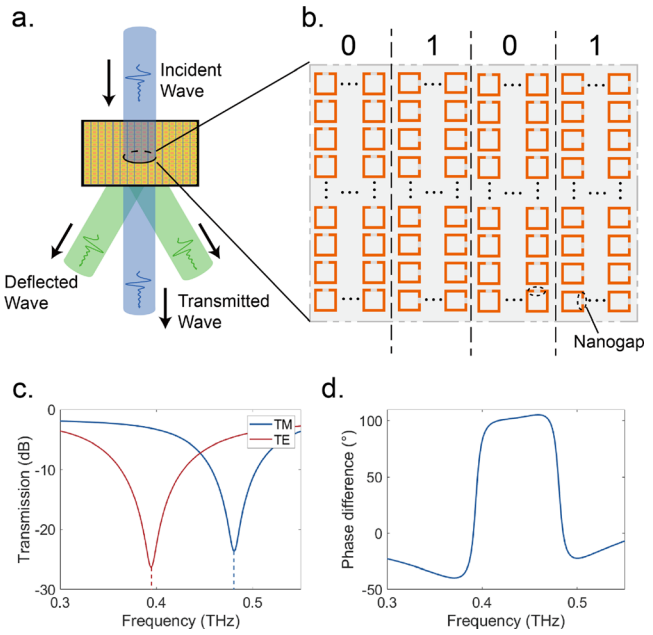

FIG. 1. Schematic diagram of the (a) beam-splitting device functionality and (b) pattern design. Device simulation design results, including (c) transmission spectra for incident waves with two different polarizations and (d) phase difference between the two polarizations.

nonlinear phenomena within the semiconductor material (e.g., GaAs or Si), including impact ionization[26,27] and intervalley scattering.[28] Consequently, the resonance frequency would shift from f_1 to f_2, while the resonance frequency remains f_2 when the incident wave is TE-polarized. This could be explained by the evolution of the resonance mode of the SRR unit (see supplementary material Chap. 3). Details on other structural and operational attributes of the units can be found in Refs. 29 and 30, in which we reported the similar SRRs on a high-resistance silicon substrate without pattern or functional design. Compared to Si, GaAs has a much shorter carrier lifetime, which offers potential ultrafast characteristics.

The design of the unit cell is performed with the electromagnetic simulation method (see supplementary material Chap. 1 for details). The transmission spectra are depicted in Fig. 1(c), along with the phase difference illustrated in Fig. 1(d). The simulation results indicate resonant peaks at approximately 0.4 and 0.5 THz for each polarization condition. The designed frequency range was chosen based on the central frequency of the strong-field THz radiation source we constructed here, which is 0.45 THz [see Fig. 3(f) for the spectrum].

The final designed parameters include the following: s-SRRs' side length of 81 μm, a one-dimensional periodicity of 150 μm, a ring width of 4.5 μm, a gold thickness of approximately 80 nm, a nanogap width of 15 nm, a substrate thickness of 500 μm, and an overall metasurface size of 2×2 cm.

Having the unit design completed, we adopted the P-B phase principle for the pattern design, which is a type of polarization-related geometric phase and has been widely used in metasurface design. This principle aims to provide an additional phase to incident circularly polarized waves by geometrically rotating the light modulator. The theory remains applicable to linearly polarized waves as it can be decomposed into a combination of left-handed (LCP) and right-handed circularly polarized (RCP) waves. When the unit of metasurface rotates by an angle θ, the output of circularly polarized light can be expressed by the following equation, and the complete theoretical derivation process can be found in Refs. 31 and 32:

$$E_{R,L}(\theta) = \frac{1}{\sqrt{2}}\left(\frac{t_x + t_y}{2}\begin{bmatrix}1\\ \pm j\end{bmatrix} + \frac{t_x - t_y}{2}e^{\pm j2\theta}\begin{bmatrix}1\\ \mp j\end{bmatrix}\right). \quad (1)$$

The subscripts R and L represent RCP and LCP incident waves, respectively. The symbols $+$ and $-$ correspond to the RCP and LCP waves, respectively. It can be observed from this expression that a portion of the circularly polarized light wave is converted into circularly polarized components orthogonal to it, carrying an additional phase of 2θ.

As depicted in Fig. 1(d), the phase difference between the two designed polarization states is approximately $\pi/2$. Under this condition, we have $t_x = e^{j\pi/4}$ and $t_y = e^{-j\pi/4}$, resulting in $t_x + t_y = \sqrt{2}$ and $t_x - t_y = \sqrt{2}j$. Substituting these into Eq. (1), we can calculate the output light for linearly polarized light incident on resonator regions with orientations $\theta = 0$ and $\theta = \pi/2$, respectively. The corresponding results are given in the following equations:

$$E(0) = E_L(0) + E_R(0) = \frac{1}{\sqrt{2}}\left(\frac{\sqrt{2}}{2}\begin{bmatrix}2\\ 0\end{bmatrix} + \frac{\sqrt{2}j}{2}\left(\begin{bmatrix}1\\ -j\end{bmatrix} + \begin{bmatrix}1\\ j\end{bmatrix}\right)\right) = \begin{bmatrix}1+j\\ 0\end{bmatrix}, \quad (2)$$

$$E\left(\frac{\pi}{2}\right) = E_L\left(\frac{\pi}{2}\right) + E_R\left(\frac{\pi}{2}\right) = \frac{1}{\sqrt{2}}\left(\frac{\sqrt{2}}{2}\begin{bmatrix}2\\0\end{bmatrix} + \frac{\sqrt{2}j}{2}\left(-\begin{bmatrix}1\\-j\end{bmatrix} - \begin{bmatrix}1\\j\end{bmatrix}\right)\right) = \begin{bmatrix}1-j\\0\end{bmatrix}. \quad (3)$$

Based on the above results, we find that the THz waves emitted from the two patterns have identical amplitudes with a phase difference of $\pi/2$. In this way, by constructing a metasurface composed of two types of s-SRRs with orthogonal gap orientations to build an "imperfect" binary grating, we could achieve the beam-splitting function within the specific frequency range.

Based on the desired emission angle and the unit design parameters mentioned above, we designed the phase arrangement guided by antenna array theory (see the supplementary material, Chap. 2, for detailed calculation method). We first determined a continuous phase sequence, which was then discretized into 0 and $\pi/2$, each corresponding to one of the two unit orientations. This approach completed the design of the device. As the desired emission angle α increased, the phase variation became more significant, resulting in fewer adjacent units with the same gap orientation. For example, as illustrated in Fig. 2(f), the black dashed boxes in the optical micrograph each highlight a single column of s-SRRs. For a 30° emission angle, a single phase consists of four columns of s-SRRs. In comparison, 10° and 20° correspond to 13 and 6 columns, respectively.

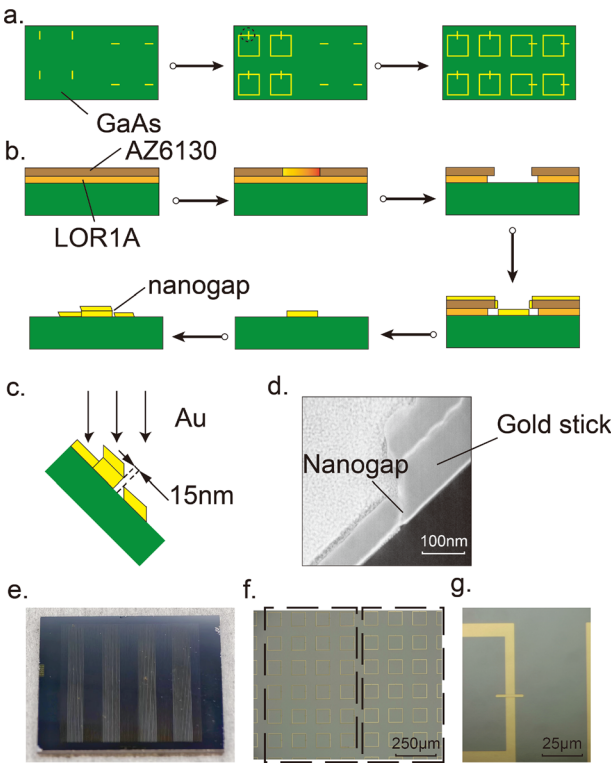

FIG. 2. (a) Multi-exposure process. (b) Complete fabrication process of the nanogap. (c)Schematic illustration of tilted evaporation method and (d) SEM image of the fabricated structure. (e) Photograph of the sample designed for a 10° emission angle, (f) optical micrograph of units with two different orientations, and (g) localized zoom-in micrograph of the nanogap and gold stick.

The device fabrication predominantly adhered to standard photolithography procedures, with the key point of the process revolving around creating nanogaps in two distinct gap orientations utilizing a titled sample evaporation method, thereby obviating the necessity for focused-ion-beam (FIB) or electron beam lithography (EBL) processes. The fabrication process encompasses three rounds of exposure and metal deposition, as delineated in Fig. 2(a). These three exposures sequentially fabricate gold sticks and the resonator rings with two different gap orientations. Figure 2(b) illustrates the process of fabricating the nanogap using the tilted sample method. The first five steps specifically detail the fabrication of gold sticks: photoresist LOR1A and AZ6130 are sequentially coated on the substrate, followed by exposure through a mask, removal of the exposed photoresist, and gold deposition to form the gold sticks (two orientations of the sticks can be processed simultaneously). Then, during the deposition of gold rings (which follows a standard process like the gold stick fabrication), the substrate with gold sticks is tilted at a specific angle, as shown in Fig. 2(c), enabling the creation of the desired nanogap. The tilted sample method has been used twice during the fabrication process: once to fabricate s-SRRs with one orientation, and once to fabricate the remaining s-SRRs with the other orientation. Different substrate tilt orientations were employed during the two exposure steps. Figure 2(d) shows the scanning electron microscope (SEM) image of the fabricated nanogap. The finalized samples are illustrated in Figs. 2(e)–2(g), with Fig. 2(e) showing the photograph of the sample with 10° emission angle.

The experiments were carried out on two self-built THz-TDS systems. Figure 3(a) depicts the weak-field THz-TDS system utilized in this research. A femtosecond fiber laser was used to power the system, and both the THz transmitting (TX) and reception (RX) modules featured low-temperature grown GaAs (LT-GaAs) photoconductive antennas. THz waves emitted from the TX module were collimated by a convex lens and then directed onto the sample as a parallel beam. The transmitted THz waves were focused onto the RX module by another convex lens and subsequently detected. The RX module was linked to a lock-in amplifier for demodulating the THz signal. A noteworthy aspect of this configuration was that the TX and RX modules were mounted on independent, programmable rotatable arms, along with the rotatable sample stage, making it particularly well-suited for detecting THz signals at different angles.

We aligned the TX, sample stage, and RX co-linearly, configuring the system in a standard arrangement to record the THz-TDS signals when nothing was placed on the sample stage. The obtained waveform is depicted in Fig. 3(c), with its corresponding frequency spectrum shown in Fig. 3(d), spanning a spectral range exceeding 1 THz.

In addition, a strong-field THz-TDS system was developed to evaluate the device's performance under strong THz electric field conditions, as illustrated in Fig. 3(b). The system employed a Ti: sapphire laser (with a wavelength of 800 nm, repetition rate of 1000 Hz, pulse width of 35 fs, and maximum output power of 5 W) as its driving source. The wavefronts of ultrafast laser pulses were tilted by a reflective grating to excite a $LiNbO_3$ crystal, thereby generating linearly vertically polarized (perpendicular to the ground) THz radiation. The THz radiation was captured using a gold-coated off-axis parabolic mirror (OAP 1), with the focal point positioned between OAP 2 and

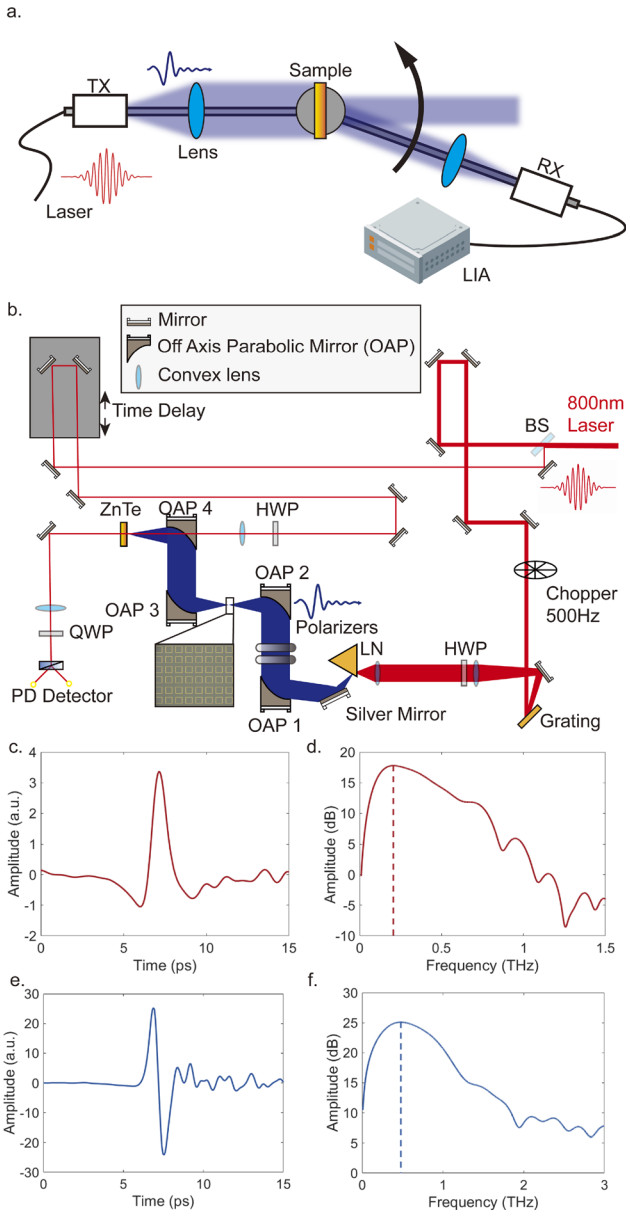

FIG. 3. Schematic diagrams of experimental systems in this work, including (a) weak-field angle-resolved TDS system and (b) strong-field TDS system. For the weak-field system, (c) the THz time-domain waveform at 0° transmission with no sample placed on the sample stage and (d) the corresponding frequency spectrum. For the strong-field system, (e) the THz time-domain waveform and (f) the corresponding spectrum when no sample was placed.

OAP 3 to achieve a substantial THz electric field, where it served as the location for sample placement. Subsequently, the THz radiation and the probe laser were co-focused onto a 1 mm ZnTe crystal. The detection of strong-field THz signals was carried out via the electro-optic sampling method. By adjusting the angle of the wire-grid polarizer pair situated between OAP 1 and OAP 2, we could adjust the incident THz electric field at the sample position.

When utilizing the laser at maximum power without placing any polarizer or sample, the obtained time-domain spectrum of THz radiation and its corresponding frequency-domain spectrum are illustrated in Figs. 3(e) and 3(f), respectively. The spectral bandwidth available is approximately 1.5 THz, with a central frequency of about 0.5 THz.

We designed and fabricated three types of samples with an emission angle of 10°, 20°, and 30°, respectively. The simulation outcomes are depicted in Figs. 4(a)–4(c), revealing a difference in the signal around 0.45 THz. Furthermore, owing to the existence of resonance peaks, the overall frequency component near 0.45 THz appeared diminished compared to neighboring frequency components.

We conducted angle-resolved measurements on the three samples using the THz-TDS system depicted in Fig. 3(a). We obtained spectra at different emission angles by performing Fourier transforms on the collected time-domain waveforms. The experimental results of the three samples are displayed in Figs. 4(d)–4(f), respectively. We could observe that there are distinct emission components around 10°, 20°, and 30°, respectively, with frequencies concentrated near 0.45 THz. The white dashed circles in the figures denote the diverted signal components, whose frequencies and diversion angles align with the simulation expectations. The gray solid line in the figure represents the distribution of the 0.45 THz frequency component (along the white dashed line) at different angles. Spectra at different emission angles are provided in supplementary material (S.6). According to the calculation from the data represented by gray solid line, for samples with emission angles of 10° and 20°, the components emitted near the designed angle

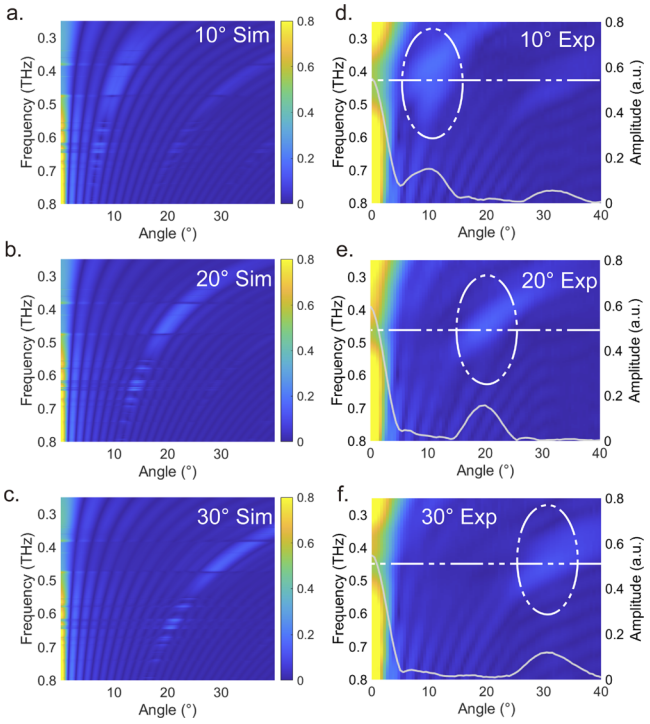

FIG. 4. Comparison of simulation results and experimental results using the rotating TDS system: (a)–(c) Simulated result of samples whose expected emission angle is 10°, 20°, and 30°, respectively, and (d)–(f) experimental result of these three samples.

constitute approximately 40% of the total; while for the sample with an emission angle of 30°, the component emitted near 30° is slightly lower.

We characterized the multi-function nano-metasurface using the strong-field THz-TDS system depicted in Fig. 3(b). The 10° emission angle sample was positioned at the THz beam's focal point, and we have ensured that only one orientation of the s-SRRs was illuminated by the focused THz beam. The beam radius at the focal point was approximately 0.8 mm, as measured by a THz camera, while the width of a single fringe in the sample was 1.95 mm. The sample was evaluated under TM-polarized and TE-polarized conditions, respectively. The incident THz electric field was adjusted by rotating a pair of wire-grid polarizers.

The transmission spectra of the sample under three electric fields of 37.5, 60, and 160 kV/cm are presented in Figs. 5(a), 5(c), and 5(e), respectively, corresponding to the spectra of the two polarization directions in Figs. 5(b), 5(d), and 5(f). Notably, under the increasing electric field, the resonance frequency of the THz transmission spectrum under the TE-polarized condition remains essentially unchanged at approximately 0.39 THz. In contrast, the resonance frequency for TM-polarized condition gradually diminished. Under the three electric field conditions, the resonance frequencies were, respectively, 0.49, 0.48, and 0.42 THz, converging toward the one associated with TE polarization. Figure 5(g) depicts alteration in phase difference between the two polarization conditions with varying electric field. The phase differences under the three conditions were approximately 55°, 45°, and 40°, respectively, indicating that as the electric field amplified, the phase difference diminished. By utilizing the resonance peak frequency of the spectra under TM-polarized condition as a characterization feature of the sample's excitation level, the variation of this feature with THz electric field is demonstrated in Fig. 5(h), where the THz electric field was calculated with the method described in Ref. 23. It is discernible that the excitation process continues to evolve from 0.49 to 0.41 THz, as the electric field varies from 37.5 to 165 kV/cm. The resonance frequency remained at 0.41 THz when the electric field reached 165 kV/cm or higher, indicating that the sample was essentially fully excited (with the frequency shift reaching saturation). In addition, we have also conducted a THz-pump THz-probe (TPTP) experiment to evaluate the ultrafast modulation potential of the device, demonstrating that the recovery time for this resonance frequency shifting is on the order of hundreds of picoseconds (see the supplementary material, Chap. 5, for detailed experiment information).

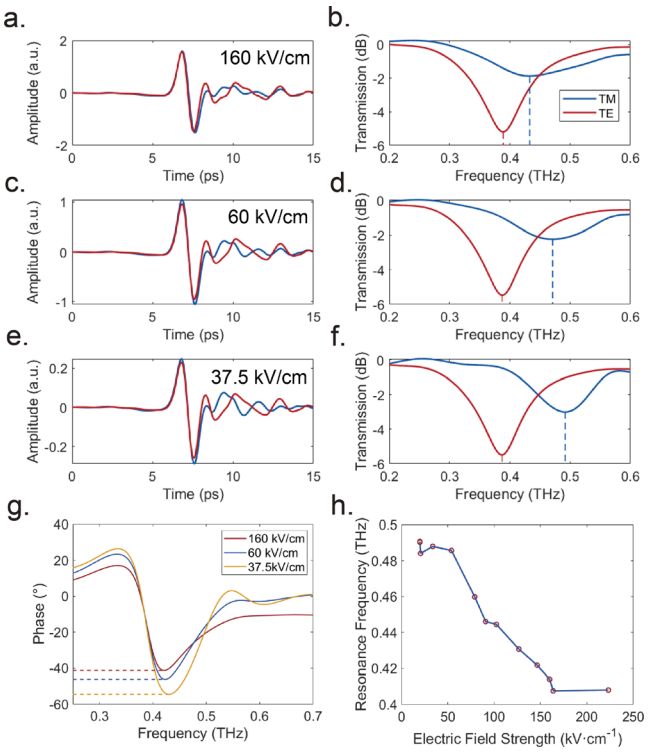

FIG. 5. Experimental results under strong-field conditions. THz pulses with peak electric field of 160, 60, and 37.5 kV/cm were respectively incident onto the sample, resulting in time-domain waveforms (a), (c), (e), and their corresponding frequency-domain spectra (b), (d), and (f). The spectra corresponding to TM and TE polarizations were acquired by manipulating the sample orientation. (g) The transmission phase difference spectra between the two polarization conditions obtained under the three electric field conditions above. Under TM-polarized incidence condition, by adjusting the THz electric field, we reached (h) the sample excitation curve, specifically, the variation of resonant frequency with changes in THz electric field.

In this work, we introduced a multi-functional THz nano-metasurface device capable of beam-splitting under weak-field conditions and nonlinear resonance frequency shifting under strong-field conditions. Furthermore, a fabrication process involved multiple exposures and a tilted sample method was developed to fabricate nano-metasurface. Using our strong-field THz-TDS system, we observed a shift in the resonance frequency from 0.5 to 0.4 THz as the incident THz electric field varied from 20 to 150 kV/cm. Additionally, the resonance frequency remains unchanged as the electric field increases beyond 165 kV/cm, indicating well excitation of the sample.

Similar to Si, GaAs demonstrates nonlinear effects under THz electric fields. However, its considerably shorter carrier lifetime compared to Si endows it with the potential for ultrafast modulation, warranting further scientific exploration.

This device further explored the modulation capability of nano-metasurfaces on THz waves with varying electric field, offering a robust research platform for integrating THz with nano-optics. The device represents a significant advancement in the development of THz self-modulation and ultrafast modulation devices and holds significant potential in communication, radar, and electromagnetic protection applications.

See the supplementary material for detailed information about the simulation method and pattern design method applied for device design, research on the resonant behaviors of unit structure, transmission spectra at different angles, and the THz-pump THz-probe experiment.

This work is supported by the National Key Research and Development Program of China (2022YFA1604402), the National Natural Science Foundation of China (U23A6002 and 92250307), and the Open Project Program of Wuhan National Laboratory for Optoelectronics (2022WNLOKF006).

AUTHOR DECLARATIONS

Conflict of Interest

The authors have no conflicts to disclose.

Author Contributions

Jianghao Li: Data curation (equal); Formal analysis (equal); Investigation (equal); Methodology (equal); Software (equal); Visualization (equal); Writing – original draft (equal). **Jiahua Cai:** Data curation (equal); Formal analysis (equal); Methodology (equal); Validation (equal); Writing – original draft (equal); Writing – review & editing (equal). **Chunyan Geng:** Investigation (equal); Validation (equal); Writing – review & editing (equal). **Deyin Kong:** Methodology (equal); Software (equal); Writing – review & editing (equal). **Mingxuan Zhang:** Visualization (equal); Writing – review & editing (equal). **Baogang Quan:** Resources (equal); Writing – review & editing (equal). **Xianxun Yao:** Project administration (equal). **Guolin Sun:** Conceptualization (equal); Funding acquisition (equal); Project administration (equal); Supervision (equal); Writing – review & editing (equal). **Xiaojun Wu:** Conceptualization (equal); Funding acquisition (equal); Project administration (equal); Supervision (equal); Writing – review & editing (equal).

DATA AVAILABILITY

The data that support the findings of this study are available from the corresponding author upon reasonable request.

REFERENCES

[1]S. Gong, D. Ping, C. Bi, Z. Zhang, S. Liang, L. Wang, H. Zeng, K. Ding, Y. Dong, H. Zhou *et al.*, "High-performance direct terahertz modulator based on resonance mode transformation for high-speed wireless communication," Appl. Phys. Lett. **121**, 231104 (2022).

[2]X. Li, T. Cui, S. Zhuang, W. Qian, L. Lin, W. Su, C. Gong, and W. Liu, "Multifunctional terahertz metamaterials based on nano-imprinting," Opt. Express **31**, 9224–9235 (2023).

[3]W. Padilla, M. Aronsson, C. Highstrete, M. Lee, A. J. Taylor, and R. Averitt, "Electrically resonant terahertz metamaterials: Theoretical and experimental investigations," Phys. Rev. B **75**, 041102 (2007).

[4]H.-T. Chen, W. J. Padilla, J. M. Zide, A. C. Gossard, A. J. Taylor, and R. D. Averitt, "Active terahertz metamaterial devices," Nature **444**, 597–600 (2006).

[5]H.-T. Chen, W. J. Padilla, M. J. Cich, A. K. Azad, R. D. Averitt, and A. J. Taylor, "A metamaterial solid-state terahertz phase modulator," Nat. Photonics **3**, 148–151 (2009).

[6]J. Lyu, S. Shen, L. Chen, Y. Zhu, and S. Zhuang, "Frequency selective fingerprint sensor: The terahertz unity platform for broadband chiral enantiomers multiplexed signals and narrowband molecular ait enhancement," PhotoniX **4**, 28 (2023).

[7]W. Xu, L. Xie, and Y. Ying, "Mechanisms and applications of terahertz metamaterial sensing: a review," Nanoscale **9**, 13864–13878 (2017).

[8]S. Shen, X. Liu, Y. Shen, J. Qu, E. Pickwell-MacPherson, X. Wei, and Y. Sun, "Recent advances in the development of materials for terahertz metamaterial sensing," Adv. Opt. Mater. **10**, 2101008 (2022).

[9]J. Li, J. Chen, D. Yan, F. Fan, K. Chen, K. Zhong, Y. Wang, Z. Tian, and D. Xu, "A review: Active tunable terahertz metamaterials," Adv. Photonics Res. **5**, 2300351 (2024).

[10]M. Samizadeh Nikoo and E. Matioli, "Electronic metadevices for terahertz applications," Nature **614**, 451–455 (2023).

[11]B. Chen, J. Wu, W. Li, C. Zhang, K. Fan, Q. Xue, Y. Chi, Q. Wen, B. Jin, J. Chen *et al.*, "Programmable terahertz metamaterials with non-volatile memory," Laser Photonics Rev. **16**, 2100472 (2022).

[12]Y. Zhang, S. Qiao, S. Liang, Z. Wu, Z. Yang, Z. Feng, H. Sun, Y. Zhou, L. Sun, Z. Chen *et al.*, "Gbps terahertz external modulator based on a composite metamaterial with a double-channel heterostructure," Nano Lett. **15**, 3501–3506 (2015).

[13]L. Cong, Y. K. Srivastava, H. Zhang, X. Zhang, J. Han, and R. Singh, "All-optical active THz metasurfaces for ultrafast polarization switching and dynamic beam splitting," Light **7**, 28 (2018).

[14]J. Guo, T. Wang, H. Zhao, X. Wang, S. Feng, P. Han, W. Sun, J. Ye, G. Situ, H.-T. Chen *et al.*, "Reconfigurable terahertz metasurface pure phase holograms," Adv. Opt. Mater. **7**, 1801696 (2019).

[15]L. Cong, P. Pitchappa, C. Lee, and R. Singh, "Active phase transition via loss engineering in a terahertz mems metamaterial," Adv. Mater. **29**, 1700733 (2017).

[16]Z. Zheng, W. Zhao, Z. Yi, L. Bian, H. Yang, S. Cheng, G. Li, L. Zeng, H. Li, and P. Jiang, "Active thermally tunable and highly sensitive terahertz smart windows based on the combination of a metamaterial and phase change material," Dalton Trans. **52**, 8294–8301 (2023).

[17]R. Xu, X. Xu, B.-R. Yang, X. Gui, Z. Qin, and Y.-S. Lin, "Actively logical modulation of mems-based terahertz metamaterial," Photonics Res. **9**, 1409–1415 (2021).

[18]D. Turchinovich, J. M. Hvam, and M. C. Hoffmann, "Self-phase modulation of a single-cycle terahertz pulse by nonlinear free-carrier response in a semiconductor," Phys. Rev. B **85**, 201304 (2012).

[19]A. D. Koulouklidis, A. C. Tasolamprou, S. Doukas, E. Kyriakou, M. S. Ergoktas, C. Daskalaki, E. N. Economou, C. Kocabas, E. Lidorikis, M. Kafesaki *et al.*, "Ultrafast terahertz self-induced absorption and phase modulation on a graphene-based thin film absorber," ACS Photonics **9**, 3075–3082 (2022).

[20]S.-H. Lee, M. Kim, Y. Roh, M.-K. Kim, and M. Seo, "Ultra-low threshold resonance switching by terahertz field enhancement-induced nanobridge," Adv. Sci. **12**, 2405225 (2024).

[21]G. Ji, H. S. Kim, S. H. Cha, H.-T. Lee, H. J. Kim, S. W. Lee, K. J. Ahn, K.-H. Kim, Y. H. Ahn, and H.-R. Park, "Terahertz virus-sized gold nanogap sensor," Nanophotonics **12**, 147–154 (2023).

[22]B. J. Kang, D. Rohrbach, F. D. Brunner, S. Bagiante, H. Sigg, and T. Feurer, "Ultrafast and low-threshold THz mode switching of two-dimensional nonlinear metamaterials," Nano Lett. **22**, 2016–2022 (2022).

[23]B. Zhang, Z. Ma, J. Ma, X. Wu, C. Ouyang, D. Kong, T. Hong, X. Wang, P. Yang, L. Chen *et al.*, "1.4-mJ high energy terahertz radiation from lithium niobates," Laser Photonics Rev. **15**, 2000295 (2021).

[24]X. Wu, D. Kong, S. Hao, Y. Zeng, X. Yu, B. Zhang, M. Dai, S. Liu, J. Wang, Z. Ren *et al.*, "Generation of 13.9-mJ terahertz radiation from lithium niobate materials," Adv. Mater. **35**, 2208947 (2023).

[25]X. Wu, "Extreme THz radiation from lithium niobite materials," Chin. Phys. Lett. **40**, 054001 (2023).

[26]K. Fan, H. Y. Hwang, M. Liu, A. C. Strikwerda, A. Sternbach, J. Zhang, X. Zhao, X. Zhang, K. A. Nelson, and R. D. Averitt, "Nonlinear terahertz metamaterials via field-enhanced carrier dynamics in GaAs," Phys. Rev. Lett. **110**, 217404 (2013).

[27]A. T. Tarekegne, K. Iwaszczuk, M. Zalkovskij, A. C. Strikwerda, and P. U. Jepsen, "Impact ionization in high resistivity silicon induced by an intense terahertz field enhanced by an antenna array," New J. Phys. **17**, 043002 (2015).

[28]F. H. Su, F. Blanchard, G. Sharma, L. Razzari, A. Ayesheshim, T. Cocker, L. Titova, T. Ozaki, J.-C. Kieffer, R. Morandotti *et al.*, "Terahertz pulse induced intervalley scattering in photoexcited GaAs," Opt. Express **17**, 9620–9629 (2009).

[29]T. Dong, S. Li, M. Manjappa, P. Yang, J. Zhou, D. Kong, B. Quan, X. Chen, C. Ouyang, F. Dai *et al.*, "Nonlinear THz-nano metasurfaces," Adv. Funct. Mater. **31**, 2100463 (2021).

[30]J. Cai, S. Chen, C. Geng, J. Li, B. Quan, and X. Wu, "Ultrafast strong-field terahertz nonlinear nanometasurfaces," Nanophotonics **12**, 2517–2526 (2023).

[31]L. Wu, J. Tao, and G. Zheng, "Controlling phase of arbitrary polarizations using both the geometric phase and the propagation phase," Phys. Rev. B **97**, 245426 (2018).

[32]J. Balthasar Mueller, N. A. Rubin, R. C. Devlin, B. Groever, and F. Capasso, "Metasurface polarization optics: Independent phase control of arbitrary orthogonal states of polarization," Phys. Rev. Lett. **118**, 113901 (2017).